Characterization of a nanopipe dislocation in GaN by means of HR-EBSD and field dislocation mechanics analysis

C. Ernould [a,b], V. Taupin [a,b], B. Beausir [a,b,*], J.J. Fundenberger [a,b], N. Maloufi [a,b], J. Guyon [a,b], E. Bouzy [a,b]

[a] Université de Lorraine, CNRS, LEM3, F-57000 Metz, France
[b] Laboratory of Excellence on Design of Alloy Metals for low-mAss, Structures (DAMAS), University of Lorraine, 57073 Metz, France

ARTICLE INFO

ABSTRACT

A nanopipe threading screw dislocation in a GaN layer is studied. A recently developed high-angular resolution electron backscatter diffraction technique, relying on a global image registration of Kikuchi patterns, is used to assess elastic strain and rotation fields in the defected area. The characterization is complemented with predictions from a piezoelectric field dislocation mechanics model of a threading screw dislocation line. In plane elastic fields are obtained at the free surface, which arise from the cancellation of the dislocation bulk shear stress field. The experimental and simulated long range fields agree qualitatively well and correspond to a screw dislocation with Burgers vector magnitude 3c = 1.56 nm.

1. Introduction

GaN is an important wide band gap semiconductor material with a large field of applications in optoelectronics and high temperature, radiofrequency, and high-power electronics. Unfortunately, the lack of suitable substrates and the necessity of heteroepitaxy generate a huge density of defects, mainly threading dislocations in GaN layers, limiting devices performances.

The present paper focuses on threading dislocations in GaN layers. More precisely, we analyze here a particular defect usually named nanopipe or giant screw dislocation [1]. Such defects were reported and investigated in the literature using various characterization techniques, such as transmission electron microscopy [2,3], large angle convergent beam electron diffraction [4], atomic force microscopy [3], multiphoton-excitation photoluminescence [5] etc. Such screw dislocations are composed of elementary Burgers vectors of the type ⟨0001⟩, parallel to the growth direction, with magnitude c = 0.52 nm. The net Burgers vector magnitude can be a multiple of c, for instance 2c [3] or 3c [1].

These dislocations are reported to possibly have hollow cores, with diameters usually in the range 5–35 nm. Such hollow cores can be seen as a release of high elastic energy at the core by creation of free surfaces [6]. GaN layers contain mostly threading dislocations, which induce long-range elastic strains, stresses, as well as piezoelectric fields [7–9].

The density of dislocation lines is the order of 5-6 $\times 10^8$ cm^{-2} in the material studied here. Hence it is possible to find isolated dislocations whose elastic fields will have a clear signature not perturbed too much by the other defects nearby. This elastic signature will be even clearer for a giant screw dislocation, because elastic strains and stresses magnitude are likely to be much larger than those of a standard screw dislocation. This will indeed be shown in the present study.

We focus our study on a nanopipe in GaN, to test a recent High-Resolution Electron Backscatter Diffraction (HR-EBSD) method developed in our team [10–12] and implemented in our analysis software ATEX [13]. Elastic strains and rotations are assessed to within 1×10^{-4} (in ideal experimental conditions) from precise knowledge of the projection geometry and the displacement field between two high-resolution ($\approx$1 Mpx) Kikuchi electron diffraction patterns, a reference one and a target one. This principle was first proposed by Wilkinson et al. [14], whose pioneering method measures local translations from small square subsets taken across both patterns by means of the Fourier-transform based cross-correlation technique. The present approach is a global one as it considers a unique and large region of interest, similarly to other recent methods [15–17]. The method differs in particular in the way the relative deformations are modelled, namely by considering a linear homography. Often used to describe projections in computer vision, the latter is measured by an iterative inverse-compositional Gauss Newton algorithm [10], modified to integrate a correction of

---
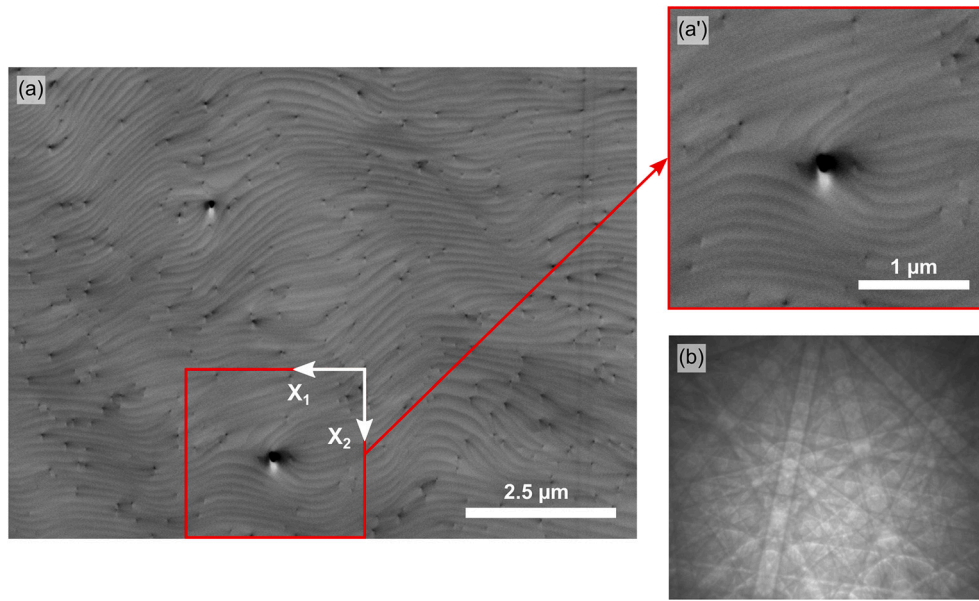
Fig. 1. (a) Backscatter electron detector image of the GaN sample and (a') close-up of the region analyzed by HR-EBSD containing a nanopipe dislocation at its center. (b) Typical electron diffraction pattern (1244 × 1024 pixels) used in the HR-EBSD analysis.

optical distortions caused by camera lenses [12]. The reader is also referred to chapters 1 to 5 in [18] for all details.

In this paper, we further applied this global HR-EBSD method to the case of what appears to be a giant screw dislocation in a GaN standard template of 3.5 μm deposited on a sapphire substrate. This defect is clearly distinguishable from the other neighboring standard dislocations in backscatter electron images (Fig. 1a). To confirm the validity of the measured elastic fields, we employ a three-dimensional piezoelectric field dislocation mechanics model of a threading screw dislocation in a GaN film [19]. The employed model is briefly presented and the simulated elastic fields are compared with those obtained by HR-EBSD. Conclusions follow.

2. Experimental methodology and modelling

2.1. Experimental data acquisition and processing

An Si doped GaN standard template of 3.5 μm thickness deposited by Metal Organic Vapour Phase Epitaxy (MOVPE) on a sapphire substrate is analyzed. A nanopipe screw dislocation, lying along a triple junction between three slightly disoriented domains, has been identified in the microscope and is shown in Fig. 1a'. A second nanopipe dislocation, slightly smaller in size, is also visible in the top of Fig. 1a but was not considered here as it is surrounded by more numerous and closer defects.

The presented experimental data are acquired with a FEG-SEM Jeol F100 equipped with an Oxford Symmetry camera. The sample to detector distance is 18 mm and the calibration is performed using the moving screen technique implemented in Aztec software. Accelerating voltage, current and aperture size are set to 15 kV, 10 nA and 50 μm, respectively. The mapped region is about 3×3 μm^2 with a step size of 40 nm, which corresponds to the commonly accepted lateral resolution limit of the EBSD technique (50 nm). Electron diffraction patterns of resolution 1244 × 1024 pixels (~19.3 μm/pixel) are recorded with an exposure time of 150 ms and 3-time frame averaging (Fig. 1b).

Raw patterns are filtered as follows: intensities are first divided by a continuous background image, then a high-pass log-filter of kernel size 101 × 101 pixels is applied, followed by a Gaussian filter of radius 1 pixel. Intensities are zero-normalized and values exceeding three times the standard deviation in absolute value are truncated. The IC-GN

algorithm considers an elliptical subset of size 1135 × 925 pixels (major and minor axes) centered on electron diffraction pattern.

Note that inside the Oxford Symmetry camera, optic fibers link the CMOS-detector to the scintillator. Though some studies have raised the concern about optical distortion in tapered fiber bundle cameras [20], the manufacturer states that the camera is distortion-free. We choose here to adhere to the latter claim. The variation of the projection geometry across the orientation map is accounted from information recorded by Oxford. We previously checked its relevance from a silicon single crystal knowing the sample tilt and map step size.

Since the measured displacement field is two-dimensional, the HR-EBSD technique is insensitive to hydrostatic dilatation. A traction-free surface condition is thus routinely applied to determine the elastic deformation gradient tensor [14]. Rotations and elastic strains are then computed considering a "finite-rotation, small strains" framework, i.e., using the left polar decomposition of the elastic transformation gradient [21]. The stress considered is the classical Cauchy stress tensor that is related to the elastic strain tensor through elastic stiffness tensor. Note that, the following elastic moduli [22] are considered for both the traction-free surface condition and the piezoelectric field dislocation mechanics model: $C_{11} = C_{22} = 390$ GPa, $C_{12} = C_{21} = 145$ GPa, $C_{13} = C_{31} = C_{23} = C_{32} = 106$ GPa, $C_{33} = 398$ GPa and $C_{44} = C_{55} = C_{66} = 105$ GPa.

### 2.2. Piezoelectric field dislocation mechanics model

The HR-EBSD measurements are confronted to predictions from a three-dimensional piezoelectric field dislocation mechanics model. The model was shown to well retrieve the elastic, but also piezoelectric, fields induced by threading dislocation lines in GaN. Hence, it is thought to be well suited here to assess the soundness of HR-EBSD measured fields. The coupled field dislocation mechanics piezoelectric model is published in [19], it is here briefly recalled. In a linear piezoelectric setting, the internal stress field and the electric displacement field are coupled through the following constitutive laws:

$$\boldsymbol{\sigma} = \mathbf{C} : \boldsymbol{\varepsilon}_e - \mathbf{f}^t.\mathbf{E} \tag{1}$$

and

$$\mathbf{D} = \boldsymbol{\mu}.\mathbf{E} + \mathbf{f}.\boldsymbol{\varepsilon}_e. \tag{2}$$

In the equation above, $\boldsymbol{\sigma}$ is the Cauchy stress tensor, $\mathbf{D}$ is the electric
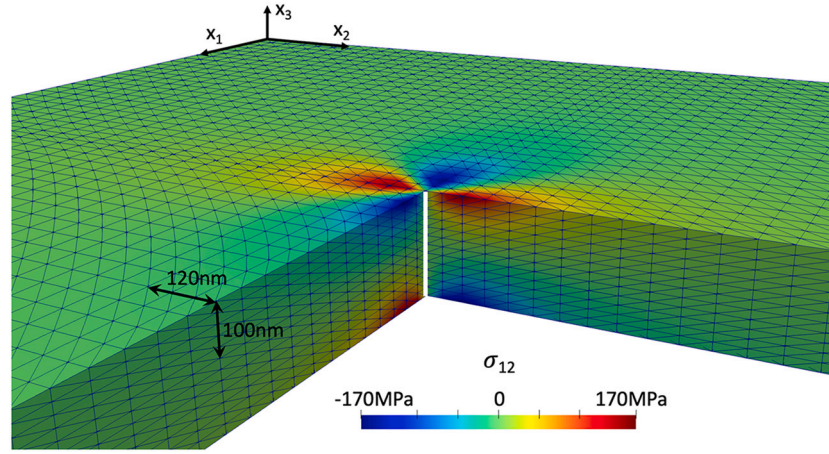
Fig. 2. Cut showing the near surface internal shear stress σ₁₂ of the threading screw dislocation predicted by the model. The dislocation line is indicated by the white solid line in the figure.

displacement vector, $\boldsymbol{\varepsilon_e}$ is the elastic strain and $\mathbf{E}$ is the electric vector. The latter is the gradient $\mathbf{E} = -\,\mathbf{grad}\,\phi$, where ϕ is the electric potential. The piezoelectric polarization vector is $\mathbf{P} = \mathbf{f}.\boldsymbol{\varepsilon_e}$. $\mathbf{C}$ is the elastic stiffness tensor, $\boldsymbol{\mu}$ the electric permittivity tensor and $\mathbf{f}$ is the matrix of piezo-electric moduli. In the absence of mobile charges (resp. inertia effects), the electric displacement vector field (resp. Cauchy stress tensor) is divergence free.

We use the Nye's dislocation density tensor $\boldsymbol{\alpha}$ to introduce in a continuous manner dislocations in the model. The Nye tensor is related to the incompatible elastic distortion by:

$$curl\ \mathbf{U_e} = \boldsymbol{\alpha}. \tag{3}$$

The incompatible elastic strain is then deduced from the symmetric part of the dislocation induced distortion $\mathbf{U_e}$. The net Burgers vector due to a distribution of Nye tensor on a surface S of unit normal $\mathbf{n}$ is:

$$\mathbf{b} = \int_S \boldsymbol{\alpha}.\mathbf{n}\ dS. \tag{4}$$

The elastic moduli used in the simulations are given above. The electric permittivity moduli are $\mu_{11} = \mu_{22} = \mu_{33} = 5.45\ 10^{11}\ \mathrm{cm^{-1}.V^{-1}}$. The piezoelectric tensor components are $f_{15} = -0.22\ \mathrm{cm^{-2}}$, $f_{31} = -0:22\ \mathrm{cm^{-2}}$ and $f_{33} = 0.44\ \mathrm{cm^{-2}}$.

The model field equations are numerically approximated by using the freeware Finite element code FreeFem++ [23]. In the forthcoming simulation, a threading dislocation line along the [0001] c direction is modelled. The c direction corresponds to the X₃ direction in the model. The X₁ and X₂ directions correspond to [11$\bar{2}$0] and [$\bar{1}$100] directions. We assign a Nye tensor component α_{33} on nodes in all (X₁, X₂) planes along a line threading the simulation box in the X₃ direction. The density value is chosen to get the Burgers vector magnitude as obtained from Eq. (4). The finite element mesh size in the (X₁, X₂) plane and near the dislocation line is taken to be the same as the EBSD step size (40 nm). It is slightly increased away from the dislocation line to avoid effects of free surfaces in the X₁ and X₂ directions on the dislocation elastic fields. In the X₃ direction, a convergence test was conducted and showed that a mesh size of 20 nm and a total thickness larger than 200 nm (here 240 nm) was necessary to properly capture the strong gradients of elastic fields near the free surfaces in the X₃ direction (Fig. 2).

(a) Monte-Carlo simulation

(b) Convolution mask in the (X₁, X₂) plane

(c) Convolution along X₃
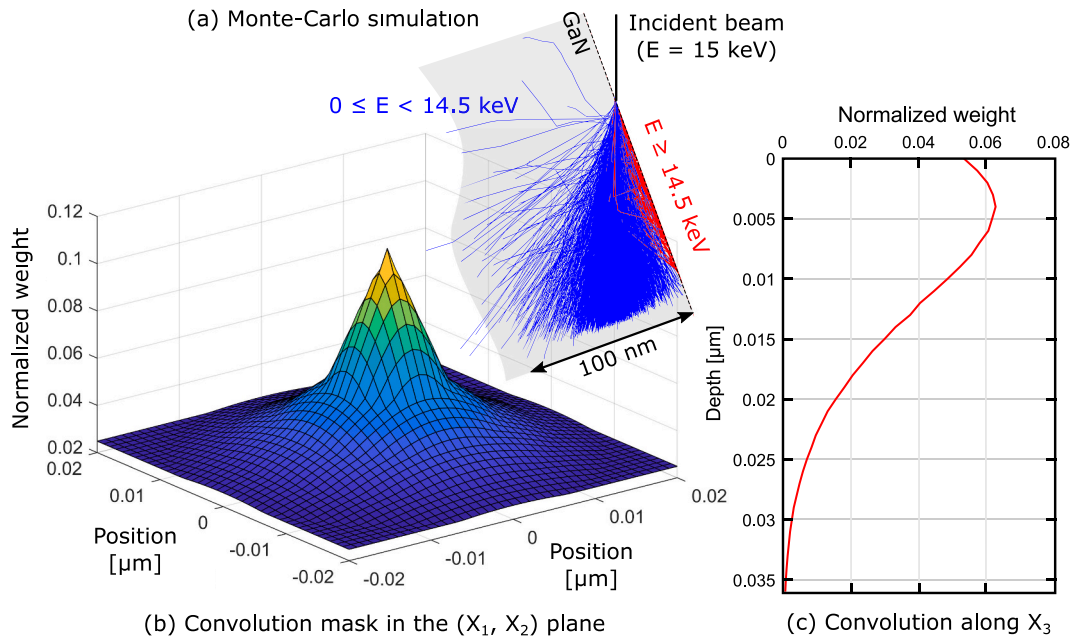
Fig. 3. (a) Monte-Carlo simulation of the backscattered electron (BE) trajectories performed with the CASINO software [25]. (b) Convolution mask in the (X₁, X₂) plane. (c) Convolution mask in depth.
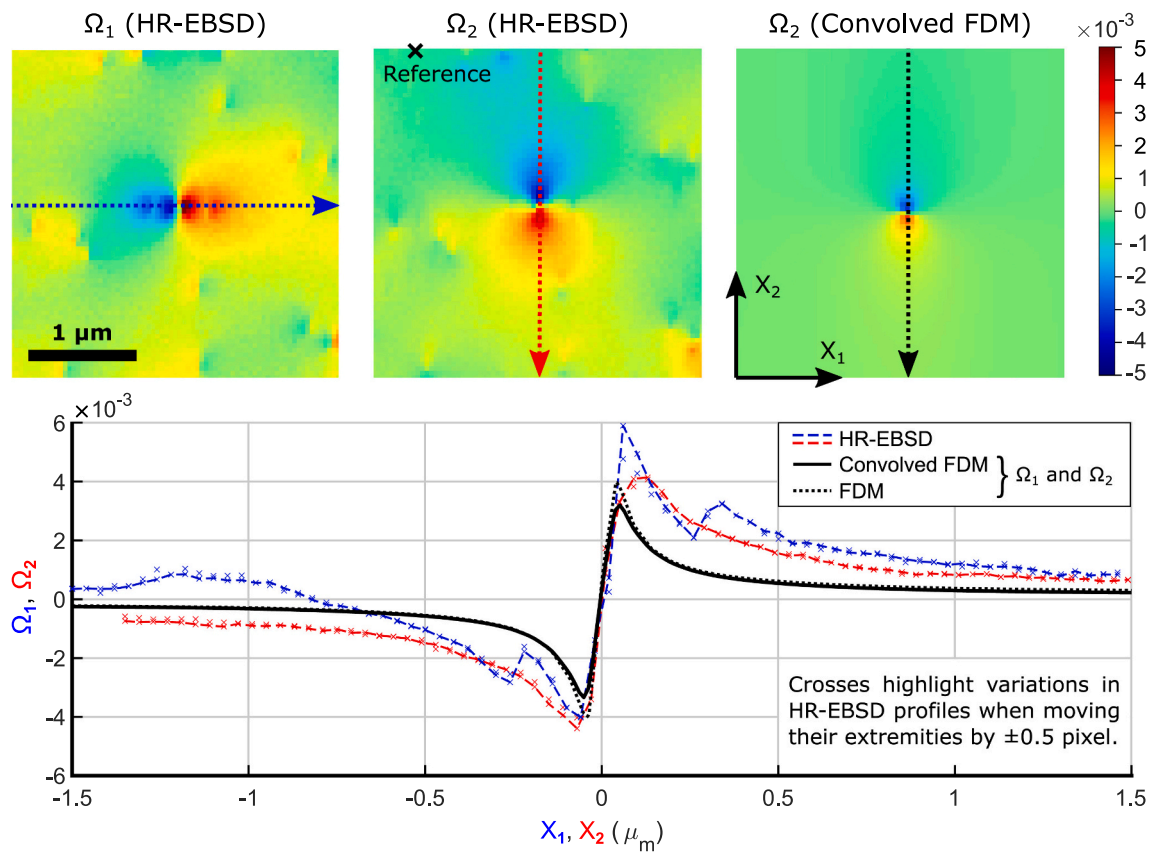
Fig. 4. Elastic rotations Ω_1 and Ω_2 (rad) of the threading screw dislocation measured by HR-EBSD and predicted by the field dislocation mechanics model.
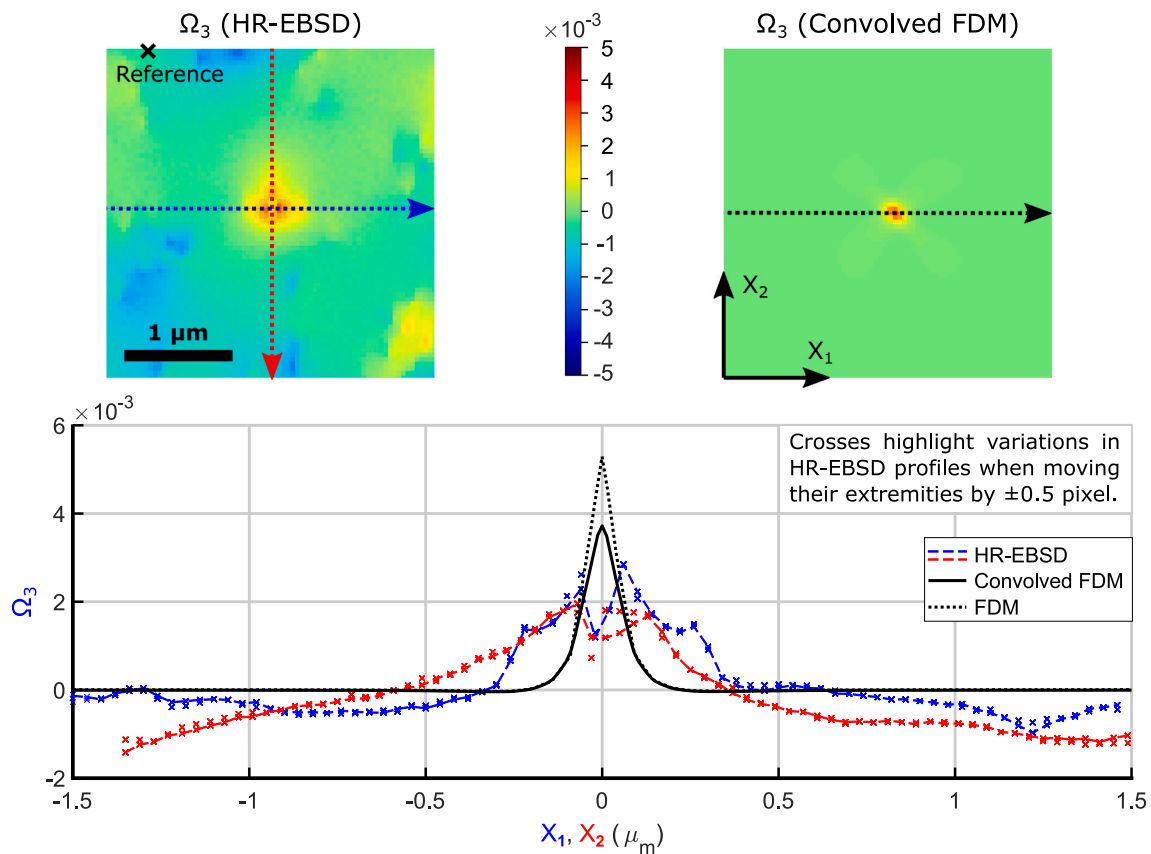

Fig. 5. Elastic rotation Ω_3 (rad) of the threading screw dislocation measured by HR-EBSD and predicted by the field dislocation mechanics model.
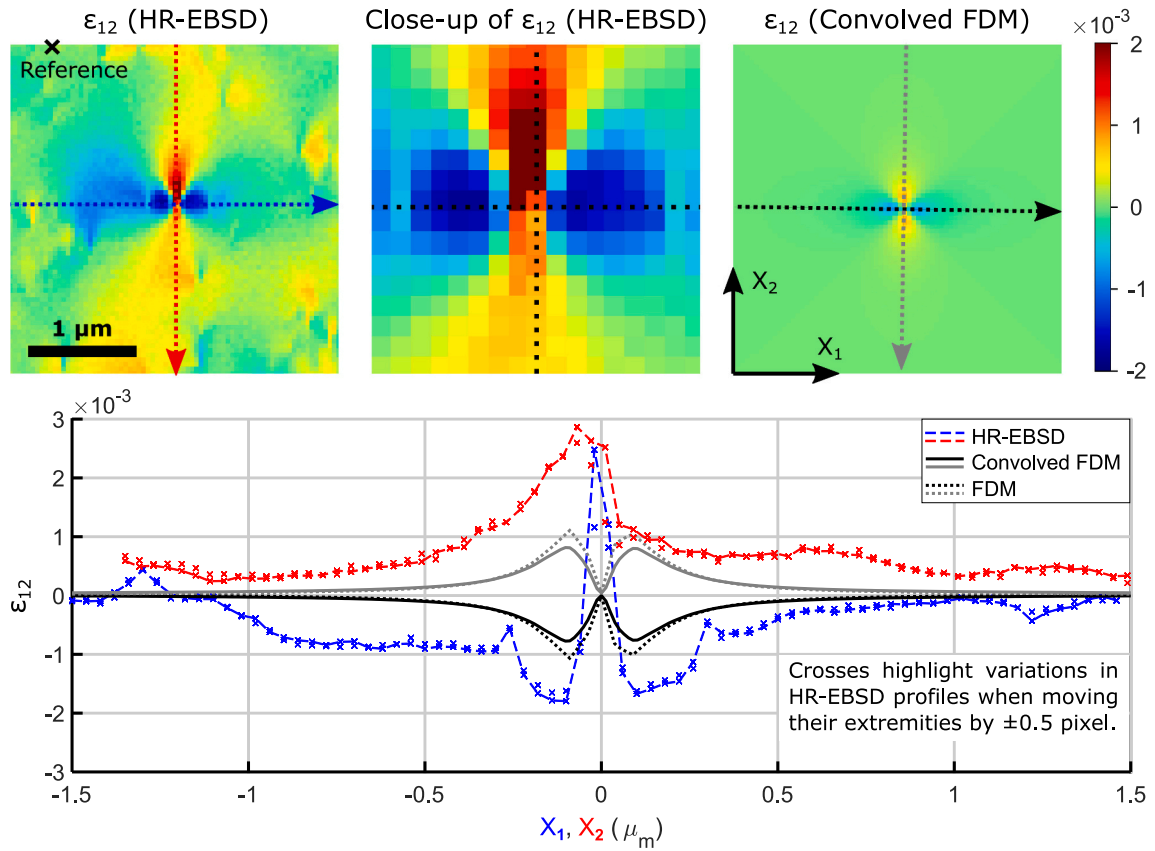
Fig. 6. Elastic strain ε_{12} of the threading screw dislocation measured by HR-EBSD and predicted by the field dislocation mechanics model.
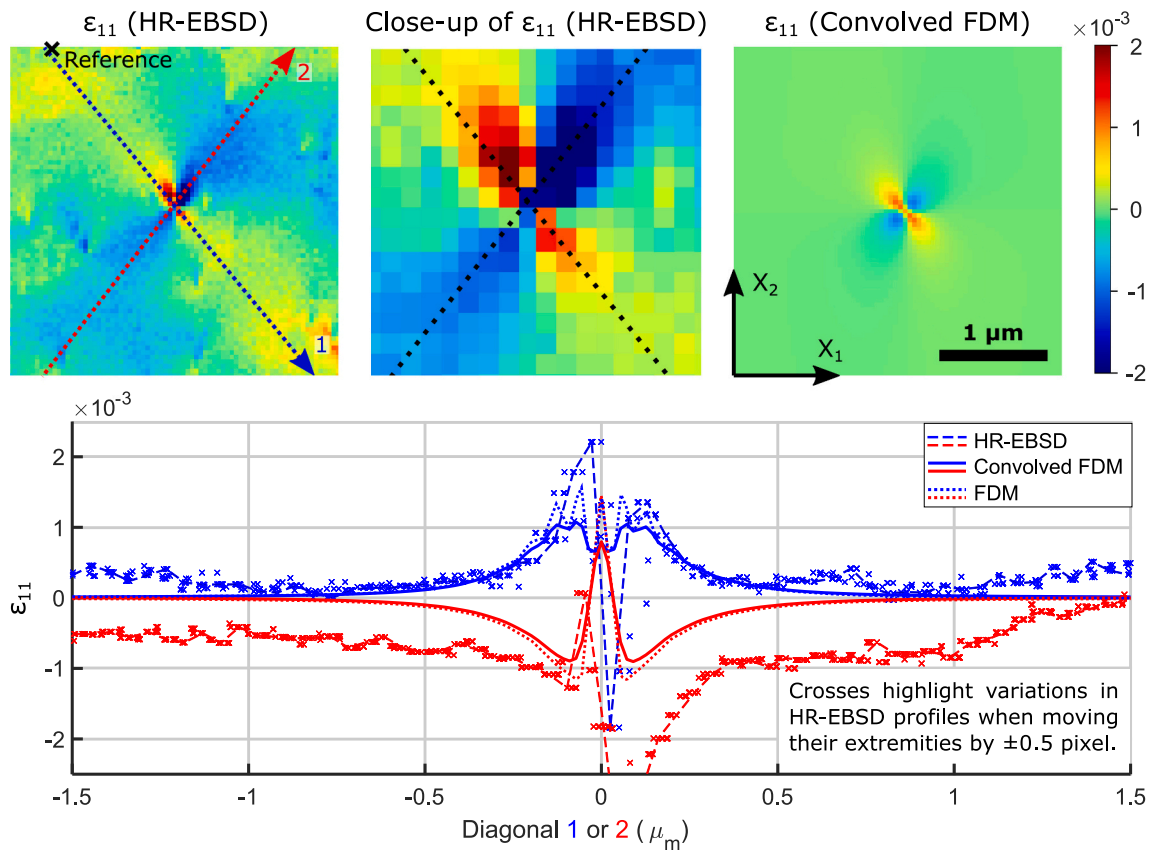

Fig. 7. Elastic strain ε_{11} of the threading screw dislocation measured by HR-EBSD and predicted by the field dislocation mechanics model.
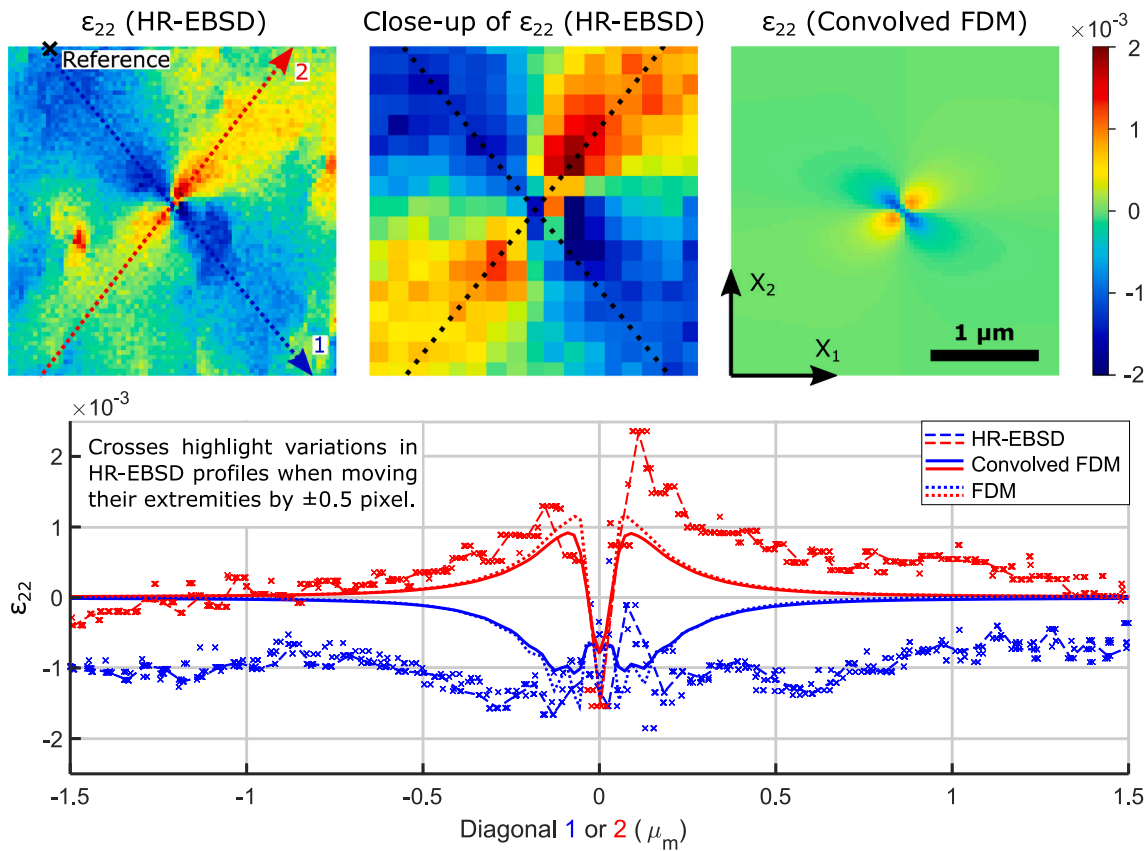
Fig. 8. Elastic strain ε_{22} of the threading screw dislocation measured by HR-EBSD and predicted by the field dislocation mechanics model.

These strong gradients originate from the cancellation of tractions due to the screw dislocation at the free surfaces. Finally, no significant piezoelectric effects are observed. This is not surprising for a screw dislocation line. More effects are expected for a threading edge dislocation [7,19]. The screw dislocation modelled here has a Burgers vector magnitude $3c = 1.56$ nm. This magnitude was chosen to fit at best the profiles and magnitudes of elastic strains and rotations obtained by HR-EBSD and shown below in Figs. 4–8. Changing the magnitude of the Burgers vector in the simulations (increase or decrease) does not change the spatial distributions of elastic fields, only their magnitude. The change in magnitude is proportional to the change in Burgers vector magnitude. We found that $b = 3c$ yields the best match.

Moreover, not shown here, we compared the simulated elastic fields at the free surface with the analytical solution for a screw dislocation in a GaN semi-infinite layer within isotropic elasticity [24]. Fields are observed to be very close, except near the dislocation line where the analytical solution tends to infinity. Also, the analytical solution for a hollow circular dislocation core [24] is not found to be relevant here because the HR-EBSD step size, 40 nm, appears to be much greater than the hollow core diameter, such that core effects on the elastic fields are barely not seen in the HR-EBSD fields.

2.3. Monte-Carlo simulation for data convolution

Since Fig. 2 shows gradients of elastic fields along the depth of the film, a Monte-Carlo simulation is performed with the CASINO software [25] to evaluate the spreading of the electron beam during HR-EBSD measurements. Then, we use these results to convolve the three-dimensional numerical strain and rotation fields accordingly, before comparing with HR-EBSD maps. A beam radius of 5 nm, a sample tilt of 70° and a total number of 10^8 electrons were set while leaving other settings to default value, the physical model in particular. The

acceleration is set to 15 keV as in our EBSD scan. Only backscattered electron having a minimum of 14.5 keV are considered for the convolution as they encompass most of the electron energy spectrum in backscatter Kikuchi diffraction [26].

Although a spread of about 100 nm along the longitudinal direction is observed in Fig. 3a, the outlet location of most electrons is less than 20 nm away from the inlet. The convolution kernel is therefore set to 40×40 nm^2 in the (X_1, X_2) plane, whose weights (Fig. 3b) are based on the distribution of the "Surface Radius of BE" in CASINO. Asymmetry due to sample tilt is ignored, its effect being assumed marginal given the voxel size of the finite-element mesh. Similarly, almost all the considered backscattered electrons stem from the first 30–40 nm in depth, but convolution is performed anyway. The mask along X_3 (Fig. 3c) is derived from the "ZMax Backscattered" distribution. It is combined with the previous one (Fig. 3b) to construct the three-dimensional kernel, whose weights are normalized (i.e., their sum is 1). This latter kernel is used to convolve the three-dimensional simulated elastic fields.

3. Results and discussion

The Figs. 4–8 compare the elastic rotations and strains as obtained from HR-EBSD analysis and with the model. Despite the screw dislocation fields obtained by HR-EBSD are locally disturbed by long range fields induced by other defects in the neighborhood, the analogy between the observed lobe polarized patterns in the elastic fields and those predicted by the model is clear.

Maps in the free surface plane are complemented by some relevant profiles along the image width (X_1), height (X_2) or diagonals, depending on the considered elastic strain or rotation component. These profile directions are indicated by dotted arrows. In some cases, a close-up allows a better visualization of their position in the vicinity of the dislocation core. To visualize the effect of the convolution, profiles extracted

from both the convolved (Convolved FDM) and the original (FDM) numerical results are plotted using solid and dotted lines in Figs. 4–8, respectively. The original numerical results correspond to the fields at the external surface.

We think that the profile comparisons confirm the soundness of the HR-EBSD measurements, despite for some fields, a faster decay with increasing distance from the dislocation line is predicted by the model. This can be particularly noticed for the elastic rotation fields (Figs. 4 and 5). There also appears to be a crater-like shape of the HR-EBSD tilt rotation field (Ω_3 in Fig. 5) in the dislocation core region, not captured by our model. We think that these discrepancies can be reasonably attributed to the effect of the dislocation core. Close-ups of elastic strain mappings obtained by HR-EBSD (Figs. 6–8) reveal spurious sign changes in experimental profiles at the dislocation line, but the values here are affected by the spatial resolution limit of the EBSD technique. The dependency with respect to the chosen path is highlighted by moving the path's extremities by ±0.5 pixels in both directions and reporting the alternative values using crosses. The effect of the dislocation core could be investigated more precisely by using an HR-TKD analysis [10,11], but it is beyond the scope of the present work.

4. Concluding remarks

To conclude, the recently developed HR-EBSD method was successfully applied to a threading screw dislocation line in a deposited GaN layer. Although the step size (40 nm) is too large to capture strong elastic field gradients at the core structure of the defect, the comparison of the elastic fields with those predicted by the field dislocation mechanics model are satisfactory and allow estimating the Burgers vector magnitude of the giant dislocation to be $3c = 1.56$ nm. This preliminary analysis constitutes a qualitative assessment of the technique as to the prediction of elastic strains and motivates for the further use of our HR-EBSD algorithm to microstructural characterizations in metals.

As previously mentioned, a quantitative analysis is limited here, mostly by the local perturbations in the elastic fields induced by neighboring defects and by the non-necessarily strain-free state of the reference point for the HR-EBSD analysis. Despite these limitations, we nevertheless show that the HR-EBSD method can capture qualitatively well such complex elastic fields, as in-plane elastic strains, normal and shear strains, which are induced by the cancellation of the dislocation bulk shear stress field at the external free surface.

The obtained results make the method appealing for the study of crystal defects in GaN, including other types of dislocations, disclinations, dislocation ensembles and disoriented domains. Finally, combined with the present piezoelectric field dislocation mechanics model, the HR-EBSD technique can indeed be used to analyze the effects of defects on piezoelectric properties.

Data availability

Data will be made available on request.

References

[1] P. Pirouz, The origin of nanopipes and micropipes in non-cubic GaN and SiC, MRS Online Proc. Libr. 512 (1998) 113–118, https://doi.org/10.1557/PROC-512-113.

[2] W. Qian, M. Skowronski, K. Doverspike, L.B. Rowland, D.K. Gaskill, Observation of nanopipes in α-GaN crystals, J. Cryst. Growth 151 (1995) 396–400, https://doi.org/10.1016/0022-0248(95)00082-8.

[3] W. Qian, G.S. Rohrer, M. Skowronski, K. Doverspike, L.B. Rowland, D.K. Gaskill, Open-core screw dislocations in GaN epilayers observed by scanning force microscopy and high-resolution transmission electron microscopy, Appl. Phys. Lett. 67 (1995) 2284–2286, https://doi.org/10.1063/1.115127.

[4] D. Cherns, W.T. Young, J.W. Steeds, F.A. Ponce, S. Nakamura, Observation of coreless dislocations in α-GaN, J. Cryst. Growth 178 (1997) 201–206, https://doi.org/10.1016/S0022-0248(97)00081-X.

[5] M. Tsukakoshi, T. Tanikawa, T. Yamada, M. Imanishi, Y. Mori, M. Uemukai, R. Katayama, Identification of Burgers vectors of threading dislocations in freestanding GaN substrates via multiphoton-excitation photoluminescence mapping, Appl. Phys. Express 14 (2021), 055504, https://doi.org/10.35848/1882-0786/abf31b.

[6] F.C. Frank, Capillary equilibria of dislocated crystals, Acta Crystallogr. 4 (1951) 497–501, https://doi.org/10.1107/S0365110X51001690.

[7] C. Shi, P.M. Asbeck, E.T. Yu, Piezoelectric polarization associated with dislocations in wurtzite GaN, Appl. Phys. Lett. 74 (1999) 573–575, https://doi.org/10.1063/1.123149.

[8] X. Han, E. Pan, Dislocation-induced fields in piezoelectric AlGaN/GaN bimaterial heterostructures, J. Appl. Phys. 112 (2012), 103501, https://doi.org/10.1063/1.4765722.

[9] G. Maciejewski, S. Kret, P. Ruterana, Piezoelectric field around threading dislocation in GaN determined on the basis of high-resolution transmission electron microscopy image, J. Microsc. 223 (2006) 212–215, https://doi.org/10.1111/j.1365-2818.2006.01622.x.

[10] C. Ernould, B. Beausir, J.-J. Fundenberger, V. Taupin, E. Bouzy, Global DIC approach guided by a cross-correlation based initial guess for HR-EBSD and on-axis HR-TKD, Acta Mater. 191 (2020) 131–148, https://doi.org/10.1016/j.actamat.2020.03.026.

[11] C. Ernould, B. Beausir, J.-J. Fundenberger, V. Taupin, E. Bouzy, Characterization at high spatial and angular resolutions of deformed nanostructures by on-axis HR-TKD, Scr. Mater. 185 (2020) 30–35, https://doi.org/10.1016/j.scriptamat.2020.04.005.

[12] C. Ernould, B. Beausir, J.-J. Fundenberger, V. Taupin, E. Bouzy, Integrated correction of optical distortions for global HR-EBSD techniques, Ultramicroscopy. 221 (2021), 113158, https://doi.org/10.1016/j.ultramic.2020.113158.

[13] B. Beausir, J.-J. Fundenberger, Analysis Tools for Electron and X-ray diffraction, ATEX - software, Université de Lorraine, Metz, 2017. http://www.atex-software.eu.

[14] A.J. Wilkinson, G. Meaden, D.J. Dingley, High resolution mapping of strains and rotations using electron backscatter diffraction, Mater. Sci. Technol. 22 (2006) 1271–1278, https://doi.org/10.1179/174328406X130966.

[15] T. Vermeij, J.P.M. Hoefnagels, A consistent full-field integrated DIC framework for HR-EBSD, Ultramicroscopy. 191 (2018) 44–50, https://doi.org/10.1016/j.ultramic.2018.05.001.

[16] T.J. Ruggles, G.F. Bomarito, R.L. Qiu, J.D. Hochhalter, New levels of high angular resolution EBSD performance via inverse compositional Gauss–Newton based digital image correlation, Ultramicroscopy. 195 (2018) 85–92, https://doi.org/10.1016/j.ultramic.2018.08.020.

[17] Q. Shi, S. Roux, F. Latourte, F. Hild, Estimation of elastic strain by integrated image correlation on electron diffraction patterns, Ultramicroscopy. 199 (2019) 16–33, https://doi.org/10.1016/j.ultramic.2019.02.001.

[18] C. Ernould, B. Beausir, J.-J. Fundenberger, V. Taupin, E. Bouzy, in: Martin Hÿtch, Peter W. Hawkes (Eds.), Advances in Imaging and Electron Physics vol. 223, Elsevier, 2022.

[19] V. Taupin, C. Fressengeas, P. Ventura, M. Lebyodkin, V. Gornakov, A field theory of piezoelectric media containing dislocations, J. Appl. Phys. 115 (2014) 144902, https://doi.org/10.1063/1.4870931.

[20] M.S. Islam, R.A. Lewis, K. Uesugi, M.J. Kitchen, A high precision recipe for correcting images distorted by a tapered fiber optic, J. Instrum. 5 (2010), https://doi.org/10.1088/1748-0221/5/09/P09008. P09008–P09008.

[21] C. Maurice, J.H. Driver, R. Fortunier, On solving the orientation gradient dependency of high angular resolution EBSD, Ultramicroscopy. 113 (2012) 171–181, https://doi.org/10.1016/j.ultramic.2011.10.013.

[22] A. Polian, M. Grimsditch, I. Grzegory, Elastic constants of gallium nitride, J. Appl. Phys. 79 (1996) 3343–3344, https://doi.org/10.1063/1.361236.

[23] F. Hecht, New development in freefem++, J. Numer. Math. 20 (2012) 251–266, https://doi.org/10.1515/jnum-2012-0013.

[24] J.D. Eshelby, A.N. Stroh, CXL, Dislocations in thin plates, Lond. Edinb. Dublin Philos. Mag. J. Sci. 42 (1951) 1401–1405, https://doi.org/10.1080/14786445108560958.

[25] D. Drouin, A.R. Couture, D. Joly, X. Tastet, V. Aimez, R. Gauvin, CASINO V2.42—a fast and easy-to-use modeling tool for scanning electron microscopy and microanalysis users, Scanning. 29 (2007) 92–101, https://doi.org/10.1002/sca.20000.

[26] A. Winkelmann, T.B. Britton, G. Nolze, Constraints on the effective electron energy spectrum in backscatter Kikuchi diffraction, Phys. Rev. B 99 (2019), 064115, https://doi.org/10.1103/PhysRevB.99.064115.